

# Electron behaviour around the onset of magnetic reconnection

Susanne Flø Spinnangr<sup>1</sup>, Michael Hesse<sup>2</sup>, Paul Tenfjord<sup>3</sup>, Cecilia Norgren<sup>4</sup>, Håkon Midthun Kolstø<sup>5</sup>, Norah Kaggwa Kwagala<sup>3</sup>, Therese Moretto Jørgensen<sup>2</sup>, and Tai D Phan<sup>6</sup>

<sup>1</sup>Space Plasma Physics Group, Department of Physics and Technology, University of Bergen

<sup>2</sup>NASA Ames Research Center

<sup>3</sup>University of Bergen

<sup>4</sup>Department of Physics and Technology, University of Bergen

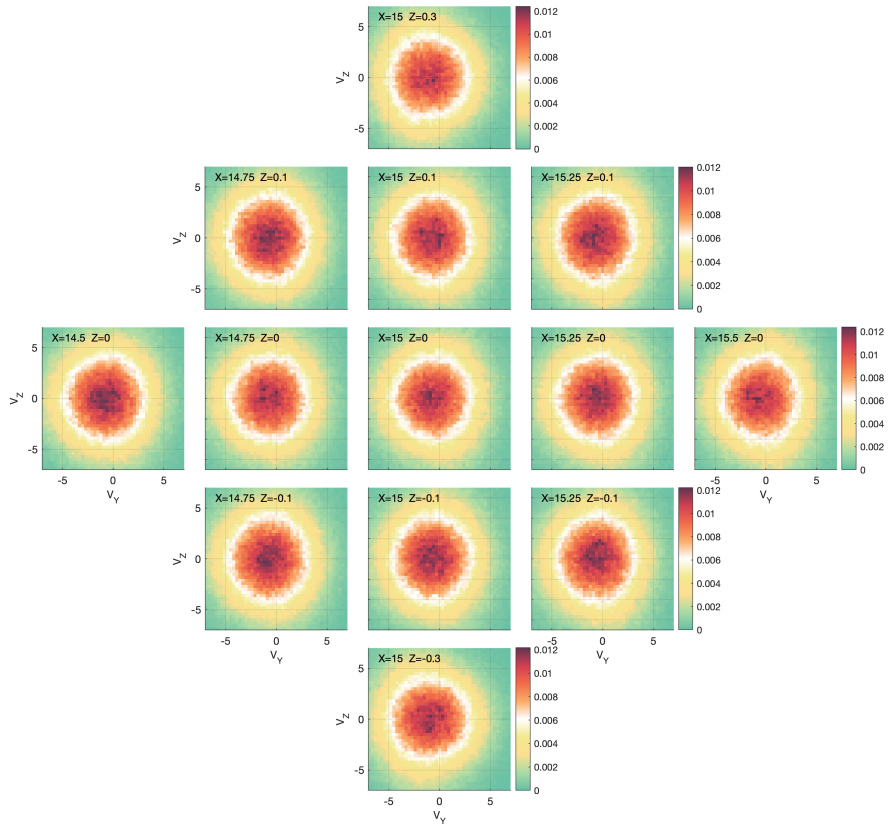
<sup>5</sup>Space Plasma Physics Group, University of Bergen

<sup>6</sup>Space Sciences Laboratory, University of California Berkeley

November 23, 2022

## Abstract

We investigate the onset of magnetic reconnection, utilizing a fully kinetic Particle-In-Cell (PIC) simulation. Characteristic features of the electron phase-space distributions immediately before reconnection onset are identified. These include signatures of pressure non-gyrotropy in the velocity distributions, and lemon shaped distributions in the in-plane velocity directions. Further, we explain how these features form through particle energization by the out-of-plane electric field. Identification of these features in the distributions can aid in analysis of data where clear signatures of ongoing reconnection are not yet present.



# Electron behaviour around the onset of magnetic reconnection

Susanne F. Spinnangr<sup>1</sup>, Michael Hesse<sup>2</sup>, Paul Tenfjord<sup>1</sup>, Cecilia Norgren<sup>1</sup>,  
Håkon M. Kolstø<sup>1</sup>, Norah K. Kwagala<sup>1</sup>, Therese Moretto Jørgensen<sup>2</sup>, Tai  
Phan<sup>3</sup>

<sup>1</sup>University of Bergen

<sup>2</sup>NASA Ames Research Center

<sup>3</sup>Space Sciences Laboratory, UC Berkeley

## Key Points:

- Electron distributions can be used to identify current sheets that are about to re-connect
- Onset signatures persist over extended spatial and temporal scales
- The particle distributions immediately preceding onset are characterized by features of non-gyrotropy and acceleration

---

Corresponding author: Susanne Flø Spinnangr, [susanne.spinnangr@uib.no](mailto:susanne.spinnangr@uib.no)

**Abstract**

We investigate the onset of magnetic reconnection, utilizing a fully kinetic Particle-In-Cell (PIC) simulation. Characteristic features of the electron phase-space distributions immediately before reconnection onset are identified. These include signatures of pressure non-gyrotropy in the velocity distributions, and lemon shaped distributions in the in-plane velocity directions. Further, we explain how these features form through particle energization by the out-of-plane electric field. Identification of these features in the distributions can aid in analysis of data where clear signatures of ongoing reconnection are not yet present.

**1 Introduction**

While magnetic reconnection is one of the most important energy conversion processes in our near space environment, on the Sun and in highly magnetized astrophysical plasmas, the question of what controls its onset is still not completely understood. Magnetic reconnection has been extensively modeled and observed in a large variety of plasma environments, such as planetary magnetospheres, the solar corona, astrophysical plasmas and in laboratories and fusion reactors on Earth (Yamada et al., 2010). If we want to understand how, where, and why magnetic reconnection occurs, we must understand what physical conditions are necessary for the onset of reconnection. It has been shown that magnetic reconnection needs thin current sheets to occur (e.g. Lui, 2004; Sitenov et al., 2019), but in-situ observations proves that this alone is not a sufficient criteria for reconnection onset (e.g. Paschmann et al., 2018; R. Wang et al., 2018; Phan et al., 2020).

The onset is difficult to study with spacecraft due to its explosive nature, and varied temporal and spatial scales. The majority of reconnection studies are done where and when the data shows clear signatures of already ongoing reconnection. These signatures include ion (e.g. Paschmann et al., 1979) and electron jets (Phan et al., 2007; Torbert et al., 2018), Hall magnetic and electric fields (M. Øieroset et al., 2001; Mozer et al., 2002; Wygant et al., 2005; Eastwood et al., 2010), and non-isotropic and non-gyrotropic particle distributions (e.g. Shuster et al., 2015; Burch, Torbert, et al., 2016; Chen, Hesse, Wang, Bessho, & Daughton, 2016; Z. Wang et al., 2019; Hesse et al., 2021).

Some simulation studies have aimed to understand the physics of reconnection onset. Hesse et al. (2001) show that the presence of non-gyrotropy in the electron pressure is necessary for the generation of the diffusive electric field in the location where the X-line will form. The electron non-gyrotropy generates a linear instability of the system which eventually causes the onset of reconnection. A thorough study of the effect of the ion to electron mass ratio and the strength of the driving, was presented in Liu et al. (2014). They found that the timing of the reconnection onset was strongly influenced by the mass ratio, thereby identifying the instability leading to reconnection onset as electron tearing. The importance of electron dynamics in reconnection onset was even further emphasized by Lu et al. (2020), who show both through observation and simulation that full scale magnetic reconnection initiates from electron-only reconnection (Phan et al., 2018) in the presence of a strong external driver.

In this study, we investigate the electron dynamics right before the initial formation of an X-line, in order to identify signatures that are indicative of an imminent onset of reconnection. Recognizing such signatures will aid in the classification of reconnecting and non-reconnecting current sheets, which can broaden our understanding of what conditions are necessary for reconnection onset. In the following section we describe our simulation setup. In section 3, we identify when onset occurs, then we discuss onset signatures in the electron phase space distributions in section 4, while section 5 is a summary and discussion about our results.

## 2 Simulation design

We simulate magnetic reconnection in the magnetotail using a fully kinetic, 2.5D Particle-In-Cell (PIC) simulation. In our coordinate system,  $x$  is the reconnection outflow direction,  $y$  is the initial current direction, and  $z$  is the inflow direction. Our simulation starts with a tail-like equilibrium (Birn et al., 1975) with oppositely directed magnetic fields and a current sheet with no perturbation. The initial magnetic field configuration is given by

$$B_x = \alpha(x) \tanh\left(\alpha(x) \frac{z}{l}\right) \quad (1)$$

$$B_z = \alpha'(x) \left( -z \tanh\left(\alpha(x) \frac{z}{l}\right) + \frac{l}{\alpha(x)} \right) \quad (2)$$

$$\alpha(x) = \left( 1 + \frac{bx}{\gamma l} \right)^{-\gamma} \quad (3)$$

where  $l = 2 d_i$  is the half-width of the current sheet,  $b = 0.05$ , and  $\gamma = 0.6$ . To establish converging flow towards the current sheet, the top, bottom and left boundaries of the simulation domain are subjected to an electric field driver, given by

$$\text{Left: } E_l = \Gamma(t) \left( \frac{z}{z_{max}} \right)^2 b_{xl} \quad (4)$$

$$\text{Top: } E_t = \Gamma(t) \left| \frac{x_{max}-x}{x_{max}} \right| b_{xt} \quad (5)$$

$$\text{Bottom: } E_b = \Gamma(t) \left| \frac{x_{max}-x}{x_{max}} \right| b_{xb} \quad (6)$$

which increases the asymptotic magnetic field strength ( $B_x$ ) through Faraday's law and leads to current sheet thinning. The  $b_x$  terms are expressions for the  $z$ -average of  $B_x$  in the boundary cells,  $\Gamma(t) = \tanh(0.1t)/\cosh^2(0.1t)$ , and  $t$  is time. The electric field driver peaks around  $t = 7$  before it falls off, such that the driving phase is over around  $t = 35$ , long before the system eventually reconnects. Similar driving mechanisms that mimic the loading of magnetic flux in the inflow regions by the solar wind have been employed in previous studies, successfully resulting in reconnection (e.g. Hesse et al., 2001; Pritchett, 2005, 2010; Liu et al., 2014).

Lengths are normalized to the ion inertial length,  $d_i = \frac{c}{\omega_{pi}}$ , where  $\omega_{pi} = \sqrt{\frac{n_0 e^2}{\epsilon_0 m_i}}$  is the ion plasma frequency with  $n_0$  being the initial current sheet density and  $m_i$  is the ion mass. Time is normalized to the inverse ion cyclotron frequency,  $\Omega_i^{-1} = \frac{m_i}{e B_0}$ , where  $B_0$  is the initial asymptotic magnetic field. We employ a time step of  $\omega_{pe} \delta t = 1$ . Densities are normalized to  $n_0$ , and velocities are normalized to the ion Alfvén velocity,  $v_A = B_0 / \sqrt{\mu_0 m_i n_0}$ . The boundary conditions are reflective in both the inflow and outflow directions. We use a total of  $6.7 \times 10^9$  macro-particles, and the size of the simulation domain is  $60 d_i \times 20 d_i$  divided into a grid of  $2048 \times 1024$  cells, leaving us with about 3200 particles per cell. The ions and electrons have a mass ratio of  $\frac{m_i}{m_e} = 100$  and their temperature ratio is  $\frac{T_e}{T_i} = 0.2$ . The ratio of the ion plasma frequency to the electron cyclotron frequency is  $\omega_{pe} / \Omega_e = 2$ .

In Figure 1 we show an overview of the in-plane magnetic field (contour lines) and out-of-plane current  $J_y$  (color), for four different times. We see how the thick current sheet becomes thinner as the magnetic field in the asymptotic regions become stronger, and that the thinning continues after the driving phase is over, until reconnection occurs. The penultimate panel in Figure 1 shows the simulation at the time we will investigate in detail in the following analysis.

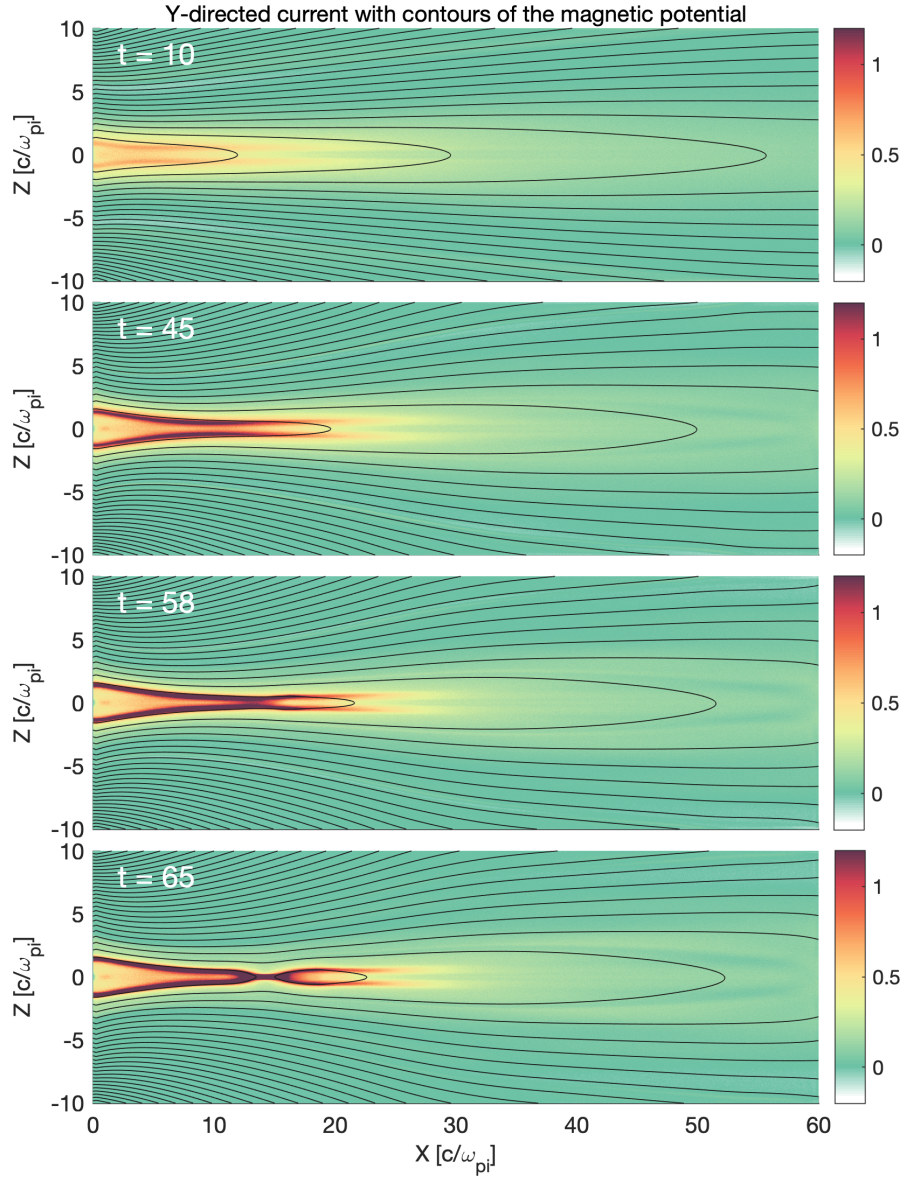


**Figure 1.** Evolution of the in-plane magnetic field (contours) and out-of-plane current density  $J_y$  (color). The current sheet becomes thinner and eventually reconnects. The penultimate panel shows the time of investigation, discussed later in the paper.

### 3 Onset of reconnection

To investigate the onset of magnetic reconnection, we must first determine when onset occurs. We follow a similar tactic as employed in (Liu et al., 2014). In our set up, the direction of  $B_z$  is initially  $< 0$  everywhere. In order for  $B_z > 0$  to appear at the neutral plane ( $z = 0$ ), reconnection must have occurred. We therefore determine the time of investigation by finding the maximum value of  $B_z(x, z = 0)$  (Figure 2a), as a function of time. An X-line forms as the max value of  $B_z$  intersects 0, which is marked in the figure with a horizontal dotted line, after which reconnection is definitely ongoing. Liu et al. (2014) determined the onset time by comparing the behaviour of  $B_z$  to a stable reference simulation in which reconnection did not occur. Onset was defined as the time when the behaviour of  $B_z$  started to deviate significantly from this reference run, in which  $B_z$  just showed a smooth change with a fairly even slope. This is similar to what we see in Figure 2a until  $t \approx 55$ . We have chosen to treat the last output time of our simulation before the X-line forms as the time of investigation, to ensure that we will see the system in the immediate pre-reconnection state. The time of investigation is  $t = 58$ , which is marked in Figure 2a with a vertical dotted line.

Next we study the off-diagonal electron pressure tensor. Magnetic reconnection can only happen in a small diffusion region where an electric field parallel to the current direction dominates the particle dynamics. This electric field is often referred to as the reconnection electric field or the diffusive electric field, and is necessary to break the frozen in condition and allow particles to diffuse across magnetic field lines. This reconnection electric field is generated through the non-gyrotropic contributions of the electron pressure tensor (Vasyliunas, 1975; Kuznetsova et al., 1998; Hesse et al., 1999, 2001). In our setup, this electric field can be expressed as

$$E_y = -\frac{1}{n_e e} \left( \frac{\partial P_{exy}}{\partial x} + \frac{\partial P_{eyz}}{\partial z} \right). \quad (7)$$

The dominating contribution around reconnection onset comes from  $\partial P_{exy}/\partial x$  (Hesse et al., 2001). Figure 2b shows  $P_{exy}$  along the x-axis at  $z = 0$  for the times leading up to the reconnection onset. A clear increase in  $P_{exy}$  starts to form at  $t = 56$ , and a significant peak is present at  $x = 15$  and  $t = 58$ , the chosen time of investigation. The existence of this peak and consequently the gradient along  $x$  around this peak confirms that our choice of investigation time is appropriate. In the following analysis of the electron behaviour, we will investigate phase space distributions centered around this peak in  $P_{exy}$ .

### 4 Particle behaviour

In the preceding section we saw that a reconnection X-line forms close to  $x = 15$  and  $z = 0$ . To investigate the electron behaviour leading up onset, we select boxes centered around this point in which we calculate the distribution functions in phase space. The boxes have  $dx = 0.125 d_i$  and  $dz = 0.05 d_i$  in each direction from their center value, such that the total length and height of each box is  $0.25d_i$  and  $0.1d_i$  respectively. The box sizes were chosen to optimize the resolution of the distributions without losing statistics by having too few particles in each box. Figures 3 and 4 show maps of the reduced distribution functions  $f_e(v_x, v_y)$  and  $f_e(v_x, v_z)$ , respectively, at  $t = 58$ . For completeness, a corresponding map in the  $v_y v_z$  plane is included as supplementary material. In the following, we will discuss features in these distributions.

As can be seen in Figure 3,  $f_e(v_x, v_y)$  is fairly similar in the different locations. This means that the features we will point out are present not only at the exact location where the X-line forms, but in a larger area around it. To aid in the analysis of the smaller scale electron behaviour, we choose to use the center distribution as an example.

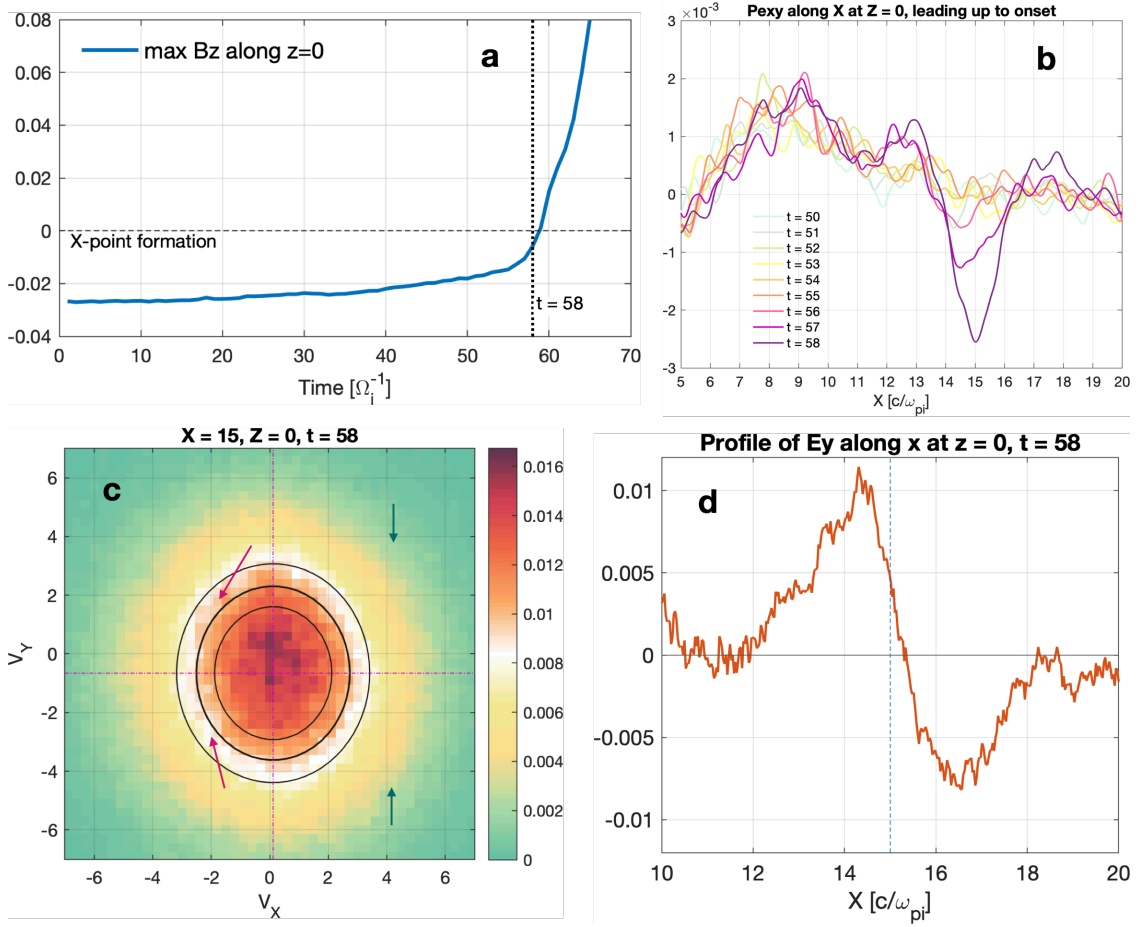


**Figure 2.** (a) Maximum value of  $B_z$  along  $z = 0$  as a function of time. When we see a significant change in the slope of this value we are close to reconnection onset. We define the time of investigation as the last output time before the formation of the X-line (indicated by the dotted line). (b) Cut through  $z = 0$  of  $P_{exy}$ , for different times leading up to the onset. The data has been averaged with a running mean in order to remove noise and extract the average behaviour. We see the necessary gradient for the generation of a diffusive electric field starts to appear and grow bigger from  $t = 56$ . (c) Electron distribution in the  $v_x v_y$  plane, at  $x = 15$ ,  $z = 0$  and  $t = 58$ . The dotted pink lines show the bulk velocity. The three black contour lines show how the distribution would look if it was purely bi-Maxwellian. (d) Cut of the reconnection electric field along  $x$  at  $z = 0$  and  $t = 58$ . The data is averaged over  $0.5 d_i$  in the  $z$ -direction in order to reduce noise. We see that the amplitude of  $E_y$  is higher to the left of where the X-line forms than to the right. This is also true for earlier times (not shown).

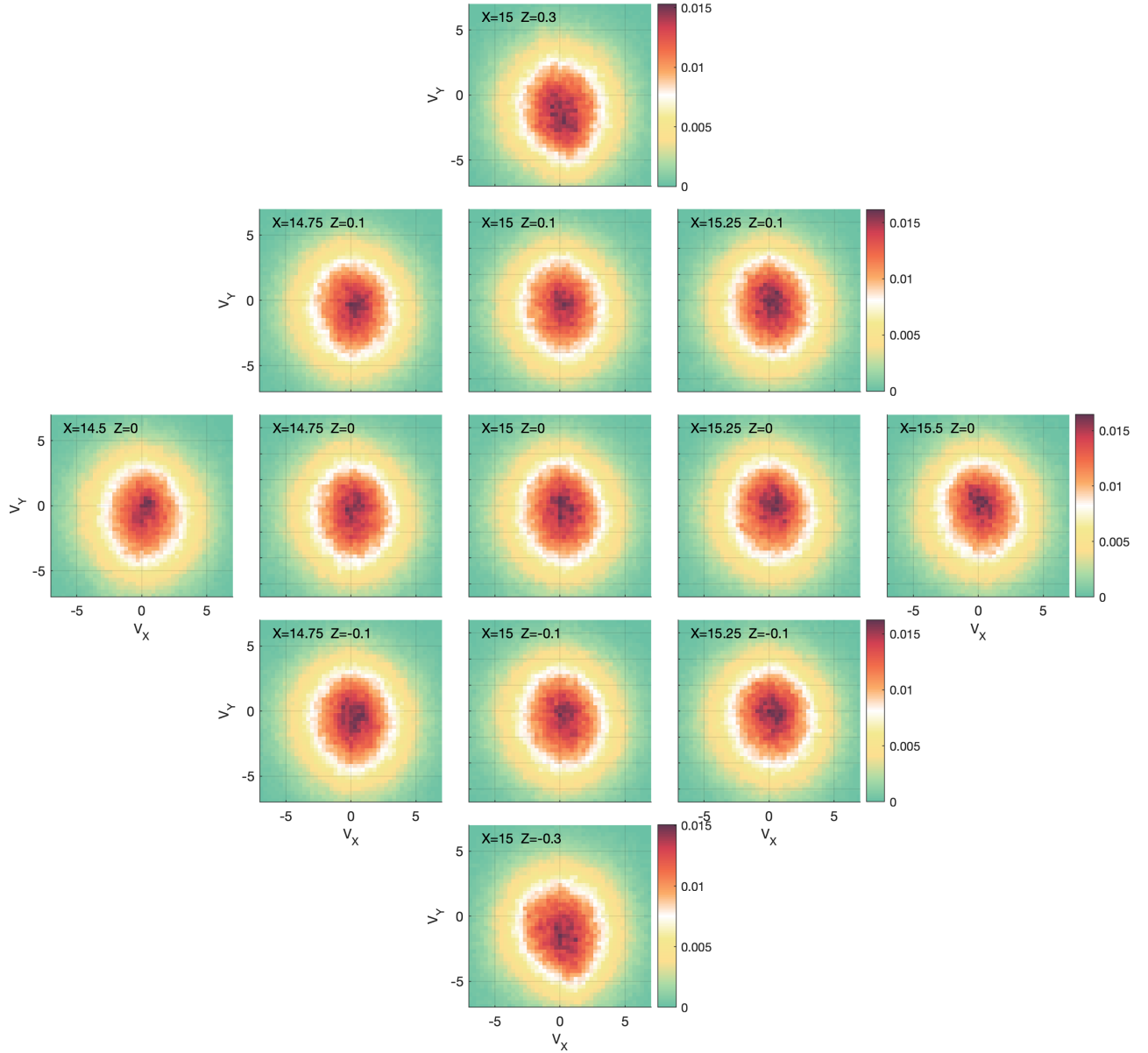


**Figure 3.** Reduced distributions  $f_e(v_x, v_y)$  centered around the point where the contribution to the reconnection electric field from the non-gyrotropic pressure reaches a maximum at  $t = 58$ . The location of the center of each box is given in the top left corner of each distribution.

147 Figure 2c shows  $f_e(v_x, v_y)$  centered around  $x = 15$  and  $z = 0$ , at  $t = 58$ . The  
 148 most prominent feature we see is a shift towards the negative  $v_y$ -direction. The two dot-  
 149 ted pink lines show the bulk flow. Previously, we found that  $P_{exy} \neq 0$  at this location  
 150 and time. We therefore expect the distribution to show non-gyrotropic features. How-  
 151 ever, since the relative magnitude of the non-gyrotropic pressure to the total pressure  
 152 is small ( $P_{exy}/P_{exx} \approx 3\%$ ), these features are subtle. To make them easier to identify,  
 153 we have overlaid the contours of a corresponding double-Maxwellian distribution, centered  
 154 at the bulk flow. As it is the higher energy parts of the distribution that provides  
 155 the largest contribution to the pressure, we are more interested in the features we see  
 156 further away from the center than the peak around the bulk flow. For particles with neg-  
 157 ative  $v_x$ , we see a clear asymmetry between the top and bottom quadrants, indicated by  
 158 the two magenta arrows. A similar, but opposite asymmetry is found for particles with  
 159 positive  $v_x$  where the green arrows are pointing. If we imagine the distribution is divided  
 160 vertically along the x-directed bulk flow into two semicircles, we see that the result of  
 161 the asymmetries is that the two halves are shifted along the  $v_y$ -direction with respect  
 162 to each other. A similar feature was found by Hesse et al. (2011) for guide field recon-  
 163 nection.

164 We can explain the shifted semicircles by taking a closer look at the history of the  
 165 particles making up the distribution. In Figure 2d we show a cut of  $E_y$  at ( $x, z = 0, t =$   
 166  $58$ ). The data has been averaged over  $\pm 0.5 d_i$  in the inflow direction to reduce noise. The  
 167 dotted blue line shows the x-location of the box in which we took the discussed distri-  
 168 bution. As we can see,  $E_y$  is positive in this location, as well as to the left of it, while  
 169 it turns negative to the right at  $x > 15.3$ . The large scale behaviour of  $E_y$  is consis-  
 170 tent with the  $\mathbf{v} \times \mathbf{B}$  drift, as the formation of a local minimum in  $B_z$  causes the frozen-  
 171 in electrons to convect earthwards on the left side of  $x = 15$  and tailwards on the right  
 172 side. However, the reversal we see between  $x = 12$  and  $x = 18$  is mostly supported  
 173 by the pressure divergence. The electrons are accelerated anti-parallel to  $E_y$ . This means  
 174 that the electrons entering the box at  $x = 15$  from the right with negative  $v_x$  are ac-  
 175 celerated in the positive y-direction, while electrons entering from the left with positive  
 176  $v_x$  are accelerated in the negative y-direction. Additionally, the magnitude of  $E_y$  is on  
 177 average slightly higher to the left of the box location than to the right. This means that  
 178 particles entering this location from the left with positive  $v_x$  have on average experienced  
 179 more acceleration by  $E_y$  than the particles coming from the right with negative  $v_x$ . This  
 180 explains the non-gyrotropic feature of  $f_e(v_x, v_y)$ .

181 This feature is visible along the  $z = 0$  plane, but as can be seen in Figure 3, it  
 182 is even clearer as we move out in the inflow direction. This is likely because the mag-  
 183 nitude of  $E_y$  is greater at the boundaries where we see a larger gradient in  $B_x$ , which  
 184 we will discuss below.

185 Figure 4 shows a map of the reduced distributions in the  $v_x v_z$ -plane, for the same  
 186 locations as in Figure 3. As with  $f_e(v_x, v_y)$ , we see that the distributions display fairly  
 187 similar features in all the locations. The most prominent feature is an elongation along  
 188 the  $v_z$ -axis around  $v_x = 0$ , resulting in lemon-shaped distributions. This tells us that  
 189 particles with none or very small  $v_x$  are experiencing larger acceleration in the z-direction.  
 190 To explain this lemon shape, we investigate how the particles are being energized.

191 In Figure 5 we again choose the distribution at  $x = 15$  and  $z = 0$  as an exam-  
 192 ple to discuss the features we see in all the distributions in Figure 4. In Figure 5a, we  
 193 have chosen an example particle to trace backwards in time to investigate how it gained  
 194 the accelerated  $v_z$ , indicated by the star. Figure 5 c through g show the particle posi-  
 195 tion, kinetic energy, and the work done on the particle by the electric field,  $-\int \mathbf{E} \cdot \mathbf{v} dt$   
 196 (including the contribution from different directions), from a time long before the on-  
 197 set up to the investigation time. We see that the particle has a general drift in the neg-  
 198 ative y-direction, while it is bouncing in the z-direction and mirroring in the x-direction.  
 199 The amplitude of the bouncing in the z-direction is fairly constant through the full time

200 interval, although we do see a general change towards smaller amplitudes from about  $t =$   
 201 54 and onward. Figure 5b shows cuts along  $z$ , through  $x = 15$ , of  $E_y$  averaged over  $0.5 d_i$   
 202 in  $x$ , plotted as a function of time. The black contour lines are the contours of the mag-  
 203 netic vector potential, indicating the motion of the magnetic field at this  $x$ . The two green  
 204 dotted lines indicate where  $z = 0.5 d_i$  for comparison with the particle position. We  
 205 see that  $E_y$  is mostly negative and close to 0 in the center, while it is positive and with  
 206 a larger amplitude further out. This is consistent with the evolution of the thinning cur-  
 207 rent layer, and the generation of outer  $y$ -directed electron current layer by the  $\mathbf{E} \times \mathbf{B}$ -  
 208 drift. The boundary between the positive and negative  $E_y$  regions is fairly stationary  
 209 until around  $t = 56$ , from when it starts to move inwards. The short burst of positive  
 210  $E_y$  in the center just before this is a transient, temporary, large-scale fluctuation that  
 211 dissipates before the time of investigation, possibly caused by reflecting waves resulting  
 212 from the driving.

213 Comparing the position of the turning point in the  $z$ -direction with the shape of  
 214 the  $E_y$  profile, we see that it coincides with the region where  $E_y$  turns positive. A closer  
 215 look at the work terms in figure 5g reveals that the increase in kinetic energy comes from  
 216 interactions with  $E_y$ , which results from the changing  $B_x$ . As the current sheet thins,  
 217  $B_x$  above and below it increases and propagates towards the center. This leads to a build  
 218 up of  $E_y$  through Faraday's law. At the turning points in  $z$ , the particle motion is par-  
 219 allel to  $E_y$ , leading to energy gain through  $\mathbf{E} \cdot \mathbf{v}$ , as can be seen in Figure 5g. This en-  
 220 ergy gain is turned into an increased  $v_z$  as the particle continues its meandering motion.  
 221 In Figure 5b, we also see the contours of the magnetic field start to move inwards and  
 222 become closer together, with an increasing rate after about  $t = 54$ . Comparing this to  
 223 the movement of the particle in  $z$ , we see the same behaviour in the amplitude of the  
 224 meandering motion. This shows that the particle bounces between the magnetic walls  
 225 of the inflow magnetic field. As the meandering in  $z$  and the propagation of the mag-  
 226 netic walls are oppositely aligned, this energy gain through  $E_y$  can also be described as  
 227 simple Fermi acceleration (Fermi, 1949; Northrop, 1963). Fermi acceleration between mov-  
 228 ing regions of increased magnetic field is a common acceleration mechanism in space plas-  
 229 mas in general, and has recently been used to describe acceleration of electrons inside  
 230 magnetic islands (Drake et al., 2006) and between merging flux ropes (Arnold et al., 2021).

## 231 5 Summary and Discussion

232 This study is part of a larger effort to understand why, when and where magnetic  
 233 reconnection occurs. To answer these questions we must understand why some current  
 234 sheets reconnect while others do not. The results of this study can be used to expand  
 235 our pool of data to investigate in this regard. By being able to identify current sheets  
 236 that are close to or at reconnection onset, data from current sheet observations that were  
 237 previously discarded since they do not show signatures of ongoing reconnection can be  
 238 included in analyses of reconnecting current sheets.

239 We identified two key signatures of reconnection onset in the electron distribution  
 240 functions. The first is non-gyrotropy in the  $v_x v_y$ -plane, seen as shifted semicircles along  
 241 the  $y$ -directed bulk flow, consistent with the necessary gradient in the non-gyrotropic elec-  
 242 tron pressure contribution to the reconnecting electric field. The second signature is lemon  
 243 shaped distributions in the  $v_x v_z$ -plane due to Fermi acceleration of the electrons bounc-  
 244 ing between the inward propagating magnetic field of the inflow regions. These distri-  
 245 bution signatures of reconnection onset are distinct from typical distributions seen dur-  
 246 ing active reconnection. Later in our simulation the electron distributions transition to  
 247 exhibit the normal signatures of reconnection, such as counter-streaming electrons in the  
 248 direction normal to the current sheet, cigar shapes in the inflow region and emerging cres-  
 249 cents (not shown).

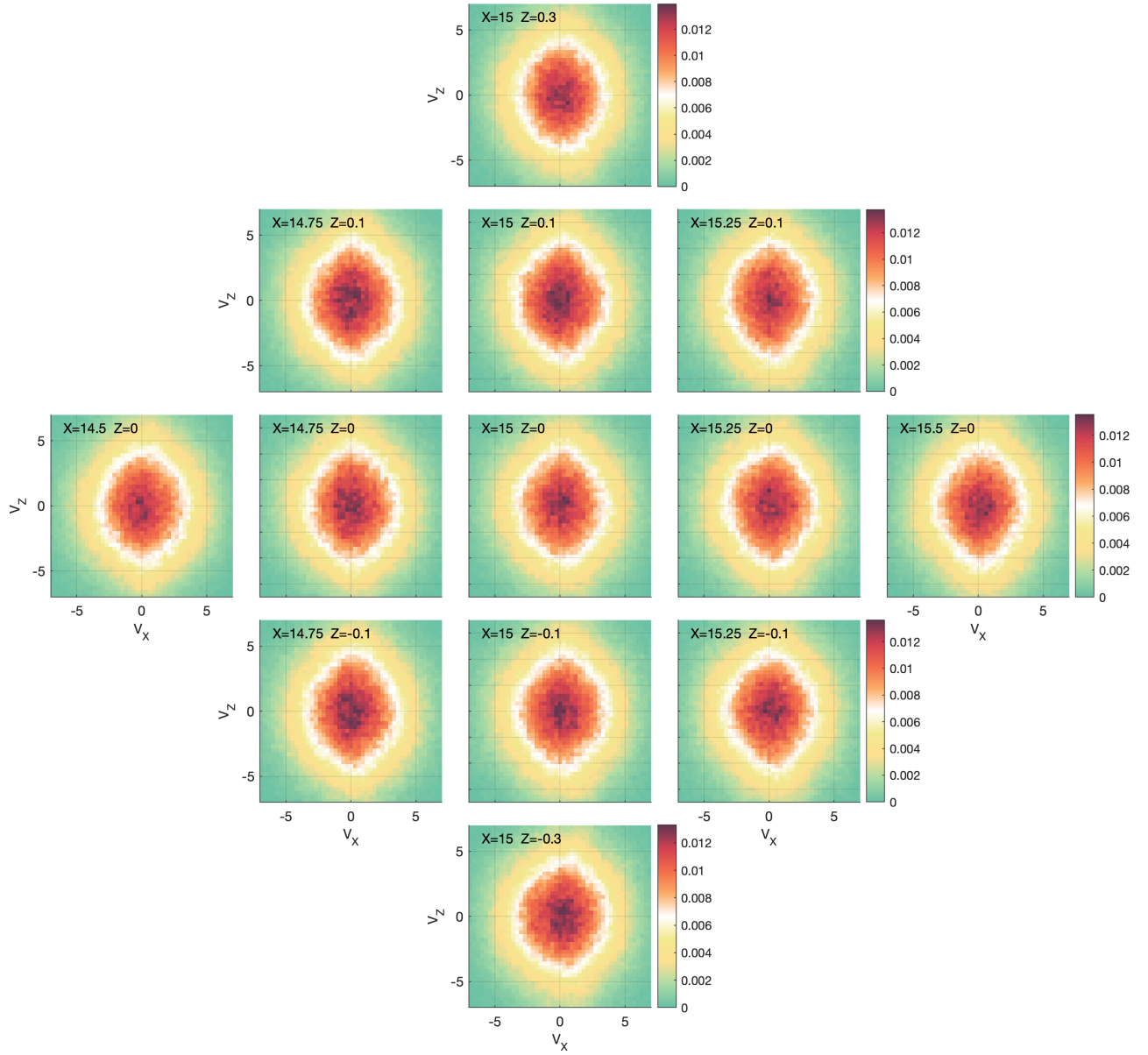


**Figure 4.** A map of  $f_e(v_x v_z)$  for the same boxes as in Figure 3 at  $t = 58$ .

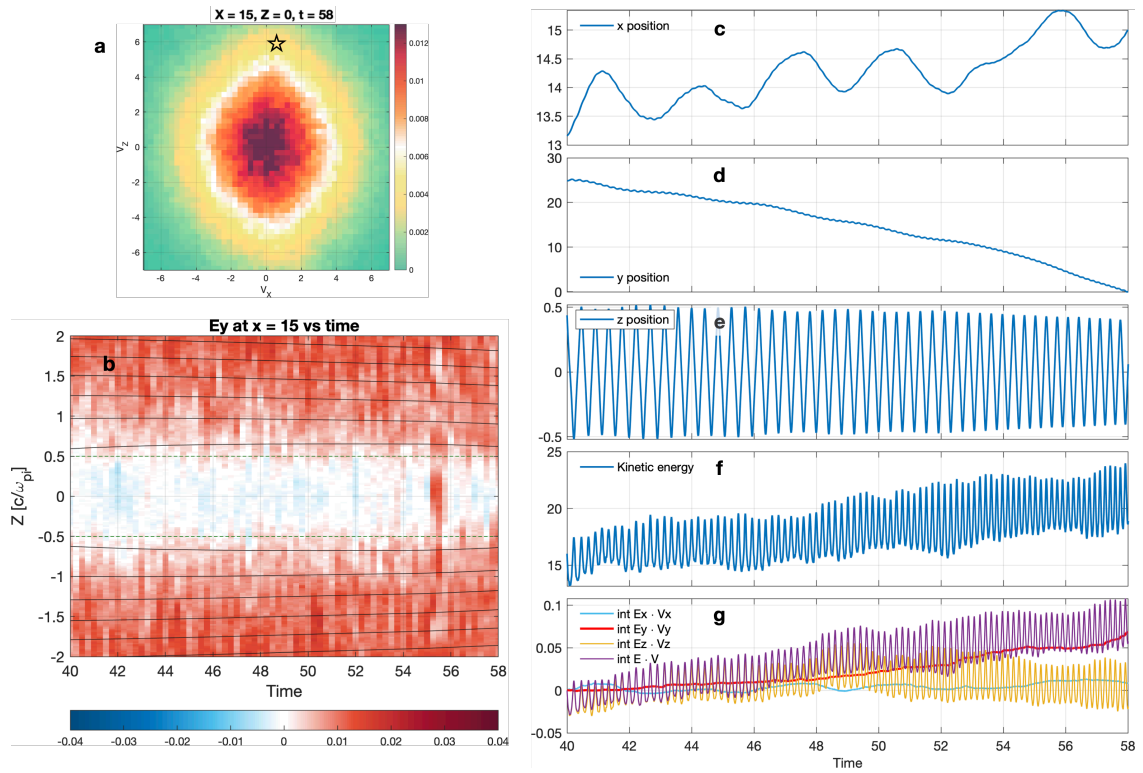


**Figure 5.** (a)  $f_e(v_x v_z)$  at  $x = 15, z = 0, t = 58$ . (b) Slices along  $z$  at  $x = 15$  of  $E_y$  (averaged over  $0.5d_i$  in  $x$ ), plotted as a function of time, with contours of the magnetic potential. (c)-(g) Position, kinetic energy and  $\int \mathbf{E} \cdot \mathbf{v} dt$  for an example particle, as a function of time.

250 In our setup, the onset signatures are clear. The temporal resolution of the Mag-  
 251 netospheric Multiscale satellites (MMS) is on electron scales (Burch, Moore, et al., 2016),  
 252 which is high enough that the signatures should be identifiable. If we assume  $B_0 = 20$  nT  
 253 and  $n_0 \sim 0.3 - 0.8$  cm<sup>-3</sup> (Toledo-Redondo et al., 2021), one ion cyclotron time in our  
 254 simulation corresponds to about 3 s, and one ion inertial length corresponds to 255 –  
 255 420 km. The identified onset signatures persist over several ion times and at least a full  
 256 ion inertial length around the forming X-line, which increases the probability of detec-  
 257 tion. Identifying currents sheets that show signs of being close to reconnection onset will  
 258 enable us to include them in research of reconnecting currents sheets, which might fur-  
 259 ther our understanding of which conditions are necessary for reconnection to occur.

## 260 Acknowledgments

261 This study was supported by NOTUR/NORSTOR under project NN9496K. CN and PT  
 262 received support from the Research Council of Norway under contract 300865. Repli-  
 263 cation data for this study is available at (Spinnangr, 2022).

## 264 References

- 265 Arnold, H., Drake, J. F., Swisdak, M., Guo, F., Dahlin, J. T., Chen, B., . . . Shen,  
 266 C. (2021). Electron Acceleration during Macroscale Magnetic Reconnection.  
 267 *Physical Review Letters*, 126(13), 135101. Retrieved from [https://doi.org/](https://doi.org/10.1103/PhysRevLett.126.135101)  
 268 10.1103/PhysRevLett.126.135101 doi: 10.1103/PhysRevLett.126.135101
- 269 Birn, J., Sommer, R., & Schindler, K. (1975). Open and closed magnetospheric  
 270 tail configurations and their stability. *Astrophysics and Space Science*, 35,  
 271 389–402.
- 272 Burch, J. L., Moore, T. E., Torbert, R. B., & Giles, B. L. (2016). *Magnetospheric*  
 273 *Multiscale Overview and Science Objectives* (Vol. 199) (No. 1-4). doi: 10.1007/  
 274 s11214-015-0164-9
- 275 Burch, J. L., Torbert, R. B., Phan, T. D., Chen, L. J., Moore, T. E., Ergun, R. E.,  
 276 . . . Chandler, M. (2016). Electron-scale measurements of magnetic reconnec-  
 277 tion in space. *Science*, 352(6290). doi: 10.1126/science.aaf2939
- 278 Chen, L. J., Hesse, M., Wang, S., Bessho, N., & Daughton, W. (2016). Elec-  
 279 tron energization and structure of the diffusion region during asymmet-  
 280 ric reconnection. *Geophysical Research Letters*, 43(6), 2405–2412. doi:  
 281 10.1002/2016GL068243
- 282 Drake, J. F., Swisdak, M., Schoeffler, K. M., Rogers, B. N., & Kobayashi, S. (2006).  
 283 Formation of secondary islands during magnetic reconnection. *Geophysical Re-*  
 284 *search Letters*, 33(13), 10–13. doi: 10.1029/2006GL025957
- 285 Eastwood, J. P., Phan, T. D., Øieroset, M., & Shay, M. A. (2010). Average prop-  
 286 erties of the magnetic reconnection ion diffusion region in the Earth’s mag-  
 287 netotail: The 2001-2005 Cluster observations and comparison with simula-  
 288 tions. *Journal of Geophysical Research: Space Physics*, 115(8), 1–13. doi:  
 289 10.1029/2009JA014962
- 290 Fermi, E. (1949). On the origin of the cosmic radiation. *Physical Review*, 75(8),  
 291 1169–1174. doi: 10.1063/1.3066619
- 292 Hesse, M., Kuznetsova, M., & Birn, J. (2001). Particle-in-cell simulations of three-  
 293 dimensional collisionless magnetic reconnection. *Journal of Geophysical Re-*  
 294 *search: Space Physics*, 106.
- 295 Hesse, M., Neukirch, T., Schindler, K., Kuznetsova, M., & Zenitani, S. (2011). The  
 296 diffusion region in collisionless magnetic reconnection. *Space Science Reviews*,  
 297 160(1-4), 3–23. doi: 10.1007/s11214-010-9740-1
- 298 Hesse, M., Norgren, C., Tenfjord, P., Burch, J. L., Liu, Y. H., Bessho, N., . . . Kwa-  
 299 gala, N. K. (2021). A New Look at the Electron Diffusion Region in Asymmet-  
 300 ric Magnetic Reconnection. *Journal of Geophysical Research: Space Physics*,

- 301 126(2), 1–16. doi: 10.1029/2020JA028456
- 302 Hesse, M., Schindler, K., Birn, J., & Kuznetsova, M. (1999). The diffusion region in  
303 collisionless magnetic reconnection. *Physics of Plasmas*, 6(5), 1781–1795. doi:  
304 10.1063/1.873436
- 305 Kuznetsova, M. M., Hesse, M., & Winske, D. (1998). Kinetic quasi-viscous and bulk  
306 flow inertia effects in collisionless magnetotail reconnection. *Journal of Geo-*  
307 *physical Research: Space Physics*, 103(A1), 199–213. doi: 10.1029/97ja02699
- 308 Liu, Y. H., Birn, J., Daughton, W., Hesse, M., & Schindler, K. (2014). Onset of  
309 reconnection in the near magnetotail: PIC simulations. *Journal of Geophysical*  
310 *Research: Space Physics*, 119(12), 9773–9789. doi: 10.1002/2014JA020492
- 311 Lu, S., Wang, R., Lu, Q., Angelopoulos, V., Nakamura, R., Artemyev, A. V., ...  
312 Wang, S. (2020). Magnetotail reconnection onset caused by electron kinet-  
313 ics with a strong external driver. *Nature Communications*, 11(1), 1–7. doi:  
314 10.1038/s41467-020-18787-w
- 315 Lui, A. T. Y. (2004). Potential Plasma Instabilities for Substorm Expansion Onsets.  
316 *Sp. Sci Rev.*, 127–206.
- 317 M. Øieroset, T. D. Phan, M. Fujimoto, R. P. Lin, & R. P. Lepping. (2001). In situ  
318 detection of reconnection in the Earth’s magnetotail. *Nature*, 412(July), 414.
- 319 Mozer, F. S., Bale, S. D., & Phan, T. D. (2002). Evidence of Diffusion Regions at a  
320 Subsolar Magnetopause Crossing. *Physical Review Letters*, 89(1), 1–4. doi: 10  
321 .1103/PhysRevLett.89.015002
- 322 Northrop, T. G. (1963). Adiabatic Charged-Particle Motion. *Reviews of Geophysics*,  
323 1(August).
- 324 Paschmann, G., Haaland, S. E., Phan, T. D., Sonnerup, B. U., Burch, J. L., Tor-  
325 bert, R. B., ... Fuselier, S. A. (2018). Large-Scale Survey of the Structure of  
326 the Dayside Magnetopause by MMS. *Journal of Geophysical Research: Space*  
327 *Physics*, 123(3), 2018–2033. doi: 10.1002/2017JA025121
- 328 Paschmann, G., Sonnerup, B. U., Papamastorakis, I., Scokpe, N., Haerendel, G.,  
329 Bame, S. J., ... Elphic, R. C. (1979). Plasma acceleration at the Earth’s  
330 magnetopause: Evidence for reconnection. *Nature*, 282(5736), 243–246. doi:  
331 10.1038/282243a0
- 332 Phan, T. D., Bale, S. D., Eastwood, J. P., Lavraud, B., Drake, J. F., Oieroset, M.,  
333 ... Velli, M. (2020). Parker Solar Probe In Situ Observations of Magnetic  
334 Reconnection Exhausts during Encounter 1. *The Astrophysical Journal Sup-*  
335 *plement Series*, 246(2), 34. doi: 10.3847/1538-4365/ab55ee
- 336 Phan, T. D., Drake, J. F., Shay, M. A., Mozer, F. S., & Eastwood, J. P. (2007).  
337 Evidence for an elongated (>60 ion skin depths) electron diffusion region dur-  
338 ing fast magnetic reconnection. *Physical Review Letters*, 99(25), 1–4. doi:  
339 10.1103/PhysRevLett.99.255002
- 340 Phan, T. D., Eastwood, J. P., Shay, M. A., Drake, J. F., Sonnerup, B. U., Fujimoto,  
341 M., ... Magnes, W. (2018). Electron magnetic reconnection without ion cou-  
342 pling in Earth’s turbulent magnetosheath. *Nature*, 557(7704), 202–206. doi:  
343 10.1038/s41586-018-0091-5
- 344 Pritchett, P. L. (2005). Externally driven magnetic reconnection in the presence  
345 of a normal magnetic field. *Journal of Geophysical Research: Space Physics*,  
346 110(A5). doi: 10.1029/2004JA010948
- 347 Pritchett, P. L. (2010). Onset of magnetic reconnection in the presence of a normal  
348 magnetic field: Realistic ion to electron mass ratio. *Journal of Geophysical Re-*  
349 *search: Space Physics*, 115(10), 1–9. doi: 10.1029/2010JA015371
- 350 Shuster, J. R., Chen, L. J., Hesse, M., Argall, M. R., Daughton, W., Torbert, R. B.,  
351 & Bessho, N. (2015). Spatiotemporal evolution of electron characteristics in  
352 the electron diffusion region of magnetic reconnection: Implications for accel-  
353 eration and heating. *Geophysical Research Letters*, 42(8), 2586–2593. doi:  
354 10.1002/2015GL063601
- 355 Sitnov, M., Birn, J., Ferdousi, B., Gordeev, E., Khotyaintsev, Y., Merkin, V., ...

- 356 Zhou, X. (2019). Explosive Magnetotail Activity. *Space Science Reviews*,  
357 215(4). Retrieved from <http://dx.doi.org/10.1007/s11214-019-0599-5>  
358 doi: 10.1007/s11214-019-0599-5
- 359 Spinnangr, S. F. (2022). *Replication data for: Electron behaviour around the onset*  
360 *of magnetic reconnection*. DataverseNO. Retrieved from [https://doi.org/10](https://doi.org/10.18710/Z2XUSW)  
361 [.18710/Z2XUSW](https://doi.org/10.18710/Z2XUSW) doi: 10.18710/Z2XUSW
- 362 Toledo-Redondo, S., André, M., Aunai, N., Chappell, C. R., Dargent, J., Fuselier,  
363 S. A., ... Vines, S. K. (2021). Impacts of Ionospheric Ions on Magnetic Reconnec-  
364 tion and Earth's Magnetosphere Dynamics. *Reviews of Geophysics*, 59(3).  
365 doi: 10.1029/2020rg000707
- 366 Torbert, R. B., Burch, J. L., Phan, T. D., Hesse, M., Argall, M. R., Shuster, J.,  
367 ... Saito, Y. (2018). Electron-scale dynamics of the diffusion region dur-  
368 ing symmetric magnetic reconnection in space. *Science*, 362(6421). doi:  
369 10.1126/science.aat2998
- 370 Vasyliunas, V. M. (1975). Theoretical models of magnetic field line merging. *Reviews*  
371 *of Geophysics*, 13(1), 303–336. doi: 10.1029/RG013i001p00303
- 372 Wang, R., Lu, Q., Nakamura, R., Baumjohann, W., Huang, C., Russell, C. T., ...  
373 Giles, B. (2018). An Electron-Scale Current Sheet Without Bursty Reconnec-  
374 tion Signatures Observed in the Near-Earth Tail. *Geophysical Research Letters*,  
375 45(10), 4542–4549. doi: 10.1002/2017GL076330
- 376 Wang, Z., Fu, H. S., Liu, C. M., Liu, Y. Y., Cozzani, G., Giles, B. L., ... Burch,  
377 J. L. (2019). Electron Distribution Functions Around a Reconnection X-  
378 Line Resolved by the FOTE Method. *Geophysical Research Letters*, 46(3),  
379 1195–1204. doi: 10.1029/2018GL081708
- 380 Wygant, J. R., Cattell, C. A., Lysak, R., Song, Y., Dombeck, J., McFadden, J.,  
381 ... Mouikis, C. (2005). Cluster observations of an intense normal compo-  
382 nent of the electric field at a thin reconnecting current sheet in the tail and  
383 its role in the shock-like acceleration of the ion fluid into the separatrix re-  
384 gion. *Journal of Geophysical Research: Space Physics*, 110(A9), 1–30. doi:  
385 10.1029/2004JA010708
- 386 Yamada, M., Kulsrud, R., & Ji, H. (2010). Magnetic reconnection. *Reviews of Mod-*  
387 *ern Physics*, 82(1), 603–664. doi: 10.1103/RevModPhys.82.603